Journal of Materials Chemistry C

PAPER

Check for updates

Photoluminescence tuning in a novel Bi³⁺/Mn⁴⁺ co-doped La₂ATiO₆:(A = Mg, Zn) double perovskite structure: phase transition and energy transfer†

Gongcheng Xing,[a] Yuxin Feng,[a] Min Pan,[a] Yi Wei,[a] Guogang Li,*[a] Peipei Dang,[b] Sisi Liang,[b] Maxim S. Molokeev,[cde] Ziyong Cheng[b] and Jun Lin ⬥ *[bf]

Red-emitting phosphors are indispensable compounds which are used to achieve a warm white light in phosphor-converted white light emitting diodes (pc-WLEDs). However, the luminous efficiency and stability of red phosphors are still big challenges. In this work, we developed red-emitting double perovskite phosphors La₂ATiO₆:Bi³⁺,Mn⁴⁺ (A = Mg, Zn) (LAT:Bi³⁺,Mn⁴⁺) and discuss the relationship between the double perovskite phosphor structure and the luminescence performance in detail. According to the Rietveld refinement results for the La₂Mg$_{(1−w)}$Zn$_w$TiO₆:Bi³⁺,Mn⁴⁺ (0 ≤ w ≤ 1) (LM$_{(1−w)}$Z$_w$T:Bi³⁺,Mn⁴⁺) solid solution, the proposed mechanism of the spectral adjustment is ascribed to the appearance of the phase transition, which results in a lower local structural symmetry of the [LaO₁₂] polyhedron and the variation of the crystal field environment for Mn⁴⁺. Notably, this is the first time that the influence of the local structure variation on the luminescence tuning in double perovskite structure phosphors has been revealed, and this could offer guidance for the development of new phosphor system. By designing Mg²⁺/Zn²⁺ cation substitution, the internal quantum efficiency (IQE) is remarkably enhanced beyond 20%. In addition, we succeeded in achieving a Bi³⁺/Mn⁴⁺ co-doped energy transfer in the double perovskite structure phosphors. Owing to the Bi³⁺ → Mn⁴⁺ energy transfer in LAT, the red emission of the Mn⁴⁺ ions could be dramatically enhanced. The energy transfer efficiency of LAT:Bi³⁺,Mn⁴⁺ eventually exceeded 90%. The IQE and the thermal stability were all enhanced by around 30% compared to the non-co-doped samples, respectively. These results indicate that the Bi³⁺ → Mn⁴⁺ energy transfer strategy could play a pivotal role in the development of highly efficient red-emitting phosphors. The performance of the fabricated pc-WLEDs devices indicates that LAT:Bi³⁺,Mn⁴⁺ could be a promising red phosphor for near ultraviolet (n-UV) based warm pc-WLEDs.

1. Introduction

Recently, phosphor-converted white light emitting diodes (pc-WLEDs) have been widely used in the lighting and display fields owing to their high efficiency, long lifetime, excellent energy conservation, environmental friendliness and so on.[1–6] The commercially available pc-WLEDs devices combine a blue InGaN LED chip and a yellow YAG:Ce³⁺ phosphor. Whereas, owing to the lack of sufficient red component in the emission spectra, the fabricated pc-WLEDs produce a cold white light with a high corresponding color temperature (CCT) (≥7750 K) and a low color rendering index (CRI) (Ra = 70–80), which causes people's eyes to feel tired after long-term usage.[7–9] To overcome this drawback, a novel n-UV InGaN based pc-WLEDs chip combining trichromatic phosphors has begun to gain attention.[10–12] Red-emitting phosphors are necessary to improve the lighting quality of pc-WLEDs. The typically used red-emitting phosphors are the Eu²⁺-activated nitrides phosphors, such as Sr₂Si₅N₈:Eu²⁺ [13] and CaSiAlN₃:Eu²⁺.[14] Although they exhibit a highly efficient red emission, their harsh synthesis conditions (high temperature and high pressure) means they have expensive

[a] Engineering Research Center of Nano-Geomaterials of Ministry of Education, Faculty of Materials Science and Chemistry, China University of Geosciences, 388 Lumo Road, Wuhan 430074, P. R. China. E-mail: ggli@cug.edu.cn

[b] State Key Laboratory of Rare Earth Resource Utilization, Changchun Institute of Applied Chemistry, Chinese Academy of Sciences, Changchun 130022, P. R. China. E-mail: jlin@ciac.ac.cn

[c] Laboratory of Crystal Physics, Kirensky Institute of Physics, FRC KSC SB RAS, Krasnoyarsk 660036, Russia

[d] Department of Physics, Far Eastern State Transport University, Khabarovsk, 680021, Russia

[e] Siberian Federal University, Krasnoyarsk, 660041, Russia

[f] School of Applied Physics and Materials, Wuyi University, Jiangmen, Guangdong, 529020, P. R. China

† Electronic supplementary information (ESI) available. See DOI: 10.1039/c8tc05171b

instrumentation costs and limits their extensive application in pc-WLEDs. Eu^{3+} always emits a linear red emission due to the characteristic 4f–4f partial spin and the forbidden transition. As its absorption is very weak in the n-UV and blue region, Eu^{3+} is not often utilized in warm pc-WLEDs owing to the low luminescence efficiency.[15,16] Thus, exploiting novel red-emitting phosphors remains to be a big challenge.

Recently, many researchers have focused on exploring non-rare earth ion activated red phosphors. Mn^{4+} mainly emits a narrow-band red light in the fluoride and oxide owing to the typical $^2E_g \rightarrow {}^4A_{2g}$ transition. Mn^{4+}-activated fluoride phosphor has been widely reported owing to its superb red emission and high quantum yield. For instance, Zhu *et al.* reported a highly efficient micrometer-sized K_2TiF_6:Mn^{4+} phosphor with a quantum yield that exceeded 98% by using a novel cation substitution strategy.[17] Fang *et al.* developed a series of narrow-band red-emitting $Na_2(Si_xGe_{1-x})F_6$:Mn^{4+} and $Na_2(Ge_yTi_{1-y})F_6$:Mn^{4+} solid solutions in which the luminous efficacy of the radiation value achieved 235 lm W_{opt}^{-1}.[18] Although Mn^{4+} doped fluoride phosphor is well matched to a n-UV or blue LED chip and exhibits excellent red-emitting properties, the abundant use of corrosive HF acid is dangerous and poisonous. Moreover, this phosphor is accompanied by serious chemical stability in air, which limits the large-scale application in WLEDs. Mn^{4+}-doped oxide phosphors could effectively avoid this serious chemical stability and are thus an appealing topic for many researchers. However, the luminescence efficiency of the Mn^{4+} ions in the oxide host need to be improved. To enhance the red emission of the Mn^{4+} ions in the oxide host, designing an appropriate energy transfer method is an effective strategy. Many rare-earth ions are good sensitizer ions, such as Ce^{3+} and Eu^{2+}. However, they can only be obtained under a reduced atmosphere. Under an air atmosphere, they are not suitable sensitizer ions for Mn^{4+}. In addition, the energy transfer can be achieved from the host to the activators, but it is hard to select appropriate hosts.[19] Recently, Bi^{3+}-doped phosphor materials have been extensively studied owing to their excellent luminescence performance and tunable emission properties.[20–22] Peng's group has made a significant amount of effort to explore Bi^{3+}-activated luminescence materials for lighting.[23–25] Bi^{3+} ions can act as a good activator, and could emit varied light in the whole visible region as determined by the crystal field environment of the host lattice due to the naked 6s and 6p orbits.[26–29] In addition to being used as an activator, Bi^{3+} could act as an excellent sensitizer,[30,31] for example, Dang *et al.* designed a $Bi^{3+} \rightarrow Eu^{3+}$ energy transfer in a $LiCa_3MgV_3O_{12}$ phosphor, and achieved full color photoluminescence tuning and enhanced red emission of Eu^{3+}.[32] $Bi^{3+} \rightarrow Mn^{4+}$ energy transfers that could also be used to enhance the red emission intensity. For instance, Zhou *et al.* reported the energy transfer induced tunable dual emission of a $Ca_3Al_4ZnO_{10}$:Bi^{3+},Mn^{4+} phosphor, which was suitable for using in agricultural fields.[31] Li *et al.* developed Bi^{3+}, Mn^{4+} co-doped $Ca_{14}Al_{10}Zn_6O_{35}$: phosphors, for which the internal quantum yields (IQYs) were as high as 98.1%.[33]

Generally, Mn^{4+} can only generate luminescence in an octahedral coordination environment. The double-perovskite $A_2BB'O_6$ (in which the A-site cation is typically an alkali, alkali earth, or rare earth cation; and the B and B'-site cation is typical a transition metal or a main group element) is a suitable matrix for doping Mn^{4+} ions to generate a red emission. It consists of a three-dimensional network by alternating the $[BO_6]$ and $[B'O_6]$ octahedra, and the A atoms occupy the interstitial space.[34] On account of the pseudo-cubic symmetry and the relative B-cation disorder in many double-perovskite compounds, the Mn^{4+} emission position changes slightly amongst the different matrix systems, such as $CaYSbO_6$:Mn^{4+} (680 nm),[35] Ba_2GdSbO_6:Mn^{4+} (687 nm),[36] $KMgLaTeO_6$:Mn^{4+} (696 nm)[37] and $BaLaMgNbO_6$:Mn^{4+} (700 nm).[38] In addition, some researchers have achieved luminescence tuning by using a cation substitution strategy, such as $(Ba,Sr)YSbO_6$:Mn^{4+} phosphor (685 nm).[39] These works indicate that the luminescence can be tuned and modified by using variation in the local coordination environment in the Mn^{4+}-activated double-perovskite $A_2BB'O_6$ phosphors. Takeda *et al.* reported La_2MgTiO_6:Mn^{4+} and La_2ZnTiO_6:Mn^{4+} red phosphors with a maximum emission at 710 nm.[40] However, the relationship between the luminescence properties and the crystal structure has not been clearly revealed. In this work, we successfully designed $La_{2(1-u/x)}ATi_{(1-z/y)}O_6$:$u/x$$Bi^{3+}$,$z/y$$Mn^{4+}$ (A = Mg^{2+}, Zn^{2+}; $0 \le u/x \le 0.03$, $0 \le z/y \le 0.01$) phosphors and a $La_2Mg_{(1-w)}Zn_wTiO_6$:$0.005Bi^{3+}$,$0.002Mn^{4+}$ ($0 \le w \le 1$) solid solution. Using Mg^{2+}/Zn^{2+} cation substitution and $Bi^{3+} \rightarrow Mn^{4+}$ energy transfer strategies, the local symmetry and coordination environment surrounding the Mn^{4+} were slightly changed, resulting in the adjustment and enhancement of the luminescence. On the basis of Rietveld refinements, when the Zn^{2+} ions gradually substitute the Mg^{2+} ions, a phase transition will appear. Local structure symmetry variation reveals the potential mechanism of the luminescence adjustment. Simultaneously, the thermal stability is evidently improved by Bi^{3+}/Mn^{4+} co-doping and the Mg^{2+}/Zn^{2+} cation substitution strategies. The electroluminescence performance also indicates that the as-prepared phosphor could act as a potential red candidate in warm pc-WLEDs. Our work could offer new insights into the effects of the local structure symmetry and the energy transfer from Bi^{3+} on the Mn^{4+} luminescence, which could offer a guidance for designing novel Mn^{4+}-doped phosphors.

2. Experimental

2.1 Materials and preparation

A series of $La_{2(1-u/x)}ATiO_6$:$u/x$$Bi^{3+}$ (LAT:$u/x$$Bi^{3+}$), $La_2ATi_{(1-z/y)}O_6$:$z/y$$Mn^{4+}$ (LAT:$z/y$$Mn^{4+}$), and $La_{2(1-u/x)}(Mg_{1-w}Zn_w)Ti_{(1-z/y)}O_6$:$u/x$$Bi^{3+}$,$z/y$$Mn^{4+}$ (A = Mg, Zn; u/x = 0–0.03, z/y = 0–0.01, w = 0, 0.25, 0.50, 0.75, 1.0) compounds were prepared using a traditional high temperature solid-state reaction in air. The $La_{2(1-u/x)}ATi_{(1-z/y)}O_6$:$u/x$$Bi^{3+}$,$z/y$$Mn^{4+}$ samples are abbreviated to be LMT:$u$$Bi^{3+}$,$z$$Mn^{4+}$ for A = Mg, LZT:$x$$Bi^{3+}$,$y$$Mn^{4+}$ for A = Zn, and L(M, Z)T:$x$$Bi^{3+}$,$y$$Mn^{4+}$ for A = (Mg, Zn), respectively. In a typical preparation process, the raw materials were La_2O_3 (Aladdin), MgO (Aladdin), TiO_2 (Aladdin), ZnO (Aladdin), Bi_2O_3 (Aladdin) and $MnCO_3$ (Aladdin), and all materials had a

purity of $\geq 99.99\%$ and were used without further processing. Stoichiometric raw materials were weighed, mixed together and ground sufficiently for 30 min in an agate mortar with a pestle, then the mixture was placed into alumina crucibles and sintered in a tube furnace at 1400 °C for 10 h in air. After cooling down to room temperature naturally, the resulting phosphor powders were successfully achieved after grinding.

2.2 pc-WLEDs device fabrication

pc-WLEDs were fabricated by combining 420 nm InGaN chips and a mixture of the representative LZT:0.005Bi^{3+},0.01Mn^{4+} phosphor and the commercially available green Ba$_3$Si$_6$O$_{12}$N$_2$:Eu^{2+} phosphor. Appropriate amounts of the phosphors were added into the epoxy resins and mixed thoroughly for 20 min. The acquired mixture was coated onto the surface of the 420 nm InGaN chips and dried at 120 °C to produce WLEDs. All of the measurements were carried out at 20 mA drive current.

2.3 Characterization

The X-ray diffraction (XRD) data for the phase purity and structural detection of the as-prepared samples were obtained by using a D8 Focus diffractometer at a scanning rate of 1° min^{-1} in the 2θ range from 10° to 120° with Ni-filtered Cu Kα ($\lambda = 1.540598$ Å). The Rietveld profile refinements of the structural models and the texture analysis was performed using the General Structure Analysis System (GSAS) software. The morphologies, energy-dispersive X-ray spectrum (EDS) and elemental mapping analysis of the samples were inspected using a field emission scanning electron microscope (FE-SEM, S-4800, Hitachi). The photoluminescence quantum yield (QY) was collected using an absolute photoluminescence quantum yield measurement system C9920-02 (Hamamatsu photonics K.K., Japan). The high-resolution transmission electron microscopy (HRTEM) images were obtained with the use of a FEI Tecnai G2 F20. The diffuse reflectance spectra (DRS) were recorded using a UV-visible diffuse reflectance spectroscopy UV-2550PC (Shimadzu Corporation, Japan). The photoluminescence excitation (PLE) and emission (PL) spectra were measured using a fluorescence spectrometer (Fluoromax-4P, Horiba Jobin Yvon, New Jersey, USA) equipped with a 150 W xenon lamp as the excitation source, and both the excitation and emission spectra were set up to be 1.0 nm with the width of the monochromator slits adjusted to 1.0 nm. The lifetimes of the as-prepared samples were detected using a Lecroy Wave Runner 6100 Digital Osilloscope (1 GHz) using a tunable laser (pulse width = 4 ns; gate = 50 ns) as the excitation source (Contimuum Sunlite OPO). The thermal stabilities of the luminescence properties were performed using a Fluoromax-4P spectrometer connected to heating equipment (TAP-02) and using a combined setup consisting of a Xe lamp, a Hamamatsu MPCD-7000 multichannel photodetector, and a computer-controlled heater. Commission Internationale de l'Eclairage chromaticity color coordinates (CIE), CRI, and the CCT of the WLEDs devices were measured by using an integrating sphere with an analyzer system (tarspec SSP6612).

3. Results and discussion

3.1 Effect of phase transition on luminescence properties

Powder X-ray diffraction provides direct evidence for the confirmation of the phase purity and crystal structure of the as-prepared compounds. Fig. 1a demonstrates the typical XRD patterns of LM$_{(1-w)}$Z$_w$T:0.005Bi^{3+},0.002Mn^{4+} ($0 \leq w \leq 1$). Obviously, the XRD patterns of the $w = 0$ and $w = 1$ samples can be easily assigned to the standard La$_2$MgTiO$_6$ (marked as LMT, ICSD No. 86852) and La$_2$ZnTiO$_6$ (marked as LZT, ICSD No. 174571) phases, respectively. As the Zn^{2+} substitution concentrations, w, increase, the XRD diffraction peaks of the LM$_{(1-w)}$Z$_w$T:0.005Bi^{3+},0.002Mn^{4+} ($0 \leq w \leq 1$) samples exhibit a monotonous shift towards the small-angle direction without any impurities, which is ascribed to the replacement of the larger Zn^{2+} ($r = 0.74$ Å, CN = 6) for Mg^{2+} ($r = 0.72$ Å, CN = 6). This result implies the successful substitution of Zn^{2+} ions into the Mg^{2+} sites and the formation of a solid solution. To further investigate the crystal structure of the solid solution, the XRD patterns of LM$_{(1-w)}$Z$_w$T:0.005Bi^{3+},0.002Mn^{4+} ($0 \leq w \leq 1$) with a 2θ range from 10° to 120° were performed with a Rietveld refinement. As shown in Fig. 1b, almost all of the reflection peaks for the $w = 0$ sample were indexed using a orthorhombic cell ($Pbnm$) with parameters close to La$_2$MgTiO$_6$ (double perovskite-type structure) except for the tiny MgO phase.[41,42] The small MgO impurity does not affect the phase structure. The other XRD Rietveld refinement patterns for the $w = 0.25$–1.0 samples are listed in Fig. S1 (ESI†). When the Zn^{2+} ions completely substitute the Mg^{2+} ions ($w = 1$), the XRD pattern could be well fitted by a monoclinic cell ($P2_1/n$) with lattice parameters close to La$_2$ZnTiO$_6$.[43] The main parameters for the processing and refinement of the LM$_{(1-w)}$Z$_w$T:0.005Bi^{3+}, 0.002Mn^{4+} samples are summarized in Table 1.

Although, minor peaks exist for the La$_2$Ti$_2$O$_7$ phase ($Pna2_1$), the refinements of all models are stable and give low R-factors (Table 1), confirming the formation of the pure phases. Furthermore, owing to the equal charge valence (+3) and the similar ionic radius between La^{3+} ($r = 1.36$ Å, CN = 12) and Bi^{3+} ($r = 1.17$ Å, CN = 8), it is suggested that Bi^{3+} occupies
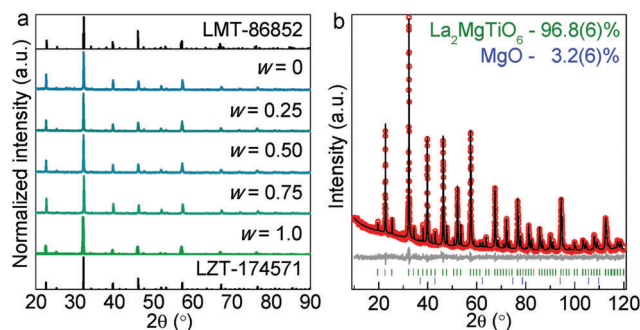
Fig. 1 (a) XRD patterns for the LM$_{(1-w)}$Z$_w$T:0.005Bi^{3+},0.002Mn^{4+} ($0 \leq w \leq 1$) samples and the standard La$_2$MgTiO$_6$ (ICSD No. 86852) and La$_2$ZnTiO$_6$ (ICSD No. 174571). (b) The rietveld refinement XRD data for the representative LMT:0.005Bi^{3+},0.002Mn^{4+} sample with the measured data (red circle), fitted data (black line), difference (grey line) and Bragg position (olive vertical bar). The blue vertical bar is the Bragg position of the MgO impurity.

13138 | J. Mater. Chem. C, 2018, 6, 13136–13147

This journal is © The Royal Society of Chemistry 2018

Table 1 Main parameters for the processing and refinement of the $LM_{(1-w)}Z_wT:0.005Bi^{3+},0.002Mn^{4+}$ ($0 \leq w \leq 1$) samples

w	Phase	Weight (%)	Space group	Cell parameters (Å, Å³)	R_{wp}, R_p (%), χ^2	R_B (%)	Impurities
0	La_2MgTiO_6	96.8(6)	$Pbnm$	$a = 5.5546(2)$ $b = 5.5592(1)$ $c = 7.8652(2)$ $V = 242.87(1)$	6.64, 5.09, 1.41	2.42	MgO
	MgO	3.2	$Fm\bar{3}m$	$a = 4.2118(3)$ $V = 74.724\,(2)$		0.72	
0.25	$La_2Mg_{0.75}Zn_{0.25}TiO_6$	94(2)	$P2_1/n$	$a = 5.5692(2)$ $b = 5.5814(2)$ $c = 7.8719(3)$ $\beta = 89.920(4)$ $V = 244.69(2)$	6.03, 4.57, 1.33	0.92	$La_2Ti_2O_7$
	$La_2Ti_2O_7$	6(2)	$Pna2_1$	$a = 25.730(6)$ $b = 7.816(1)$ $c = 5.552(1)$ $V = 1116.4(4)$		1.58	
0.5	$La_2Mg_{0.5}Zn_{0.5}TiO_6$	95(3)	$P2_1/n$	$a = 5.5712(2)$ $b = 5.5889(2)$ $c = 7.8789(3)$ $\beta = 89.961(3)$ $V = 245.32(2)$	5.99, 4.64, 1.31	0.96	$La_2Ti_2O_7$
	$La_2Ti_2O_7$	5(3)	$Pna2_1$	$a = 25.742(8)$ $b = 7.818(2)$ $c = 5.543(2)$ $V = 1115.6(5)$		1.72	
0.75	$La_2Mg_{0.25}Zn_{0.75}TiO_6$	97(2)	$P2_1/n$	$a = 5.5739(2)$ $b = 5.5960(2)$ $c = 7.8854(2)$ $\beta = 89.937(3)$ $V = 245.96(1)$	6.84, 5.11, 1.40	1.20	$La_2Ti_2O_7$
	$La_2Ti_2O_7$	3(2)	$Pna2_1$	$a = 25.732(8)$ $b = 7.815(2)$ $c = 5.542(2)$ $V = 1115.2(9)$		1.66	
1	La_2ZnTiO_6	95.8(20)	$P2_1/n$	$a = 5.5760(2)$ $b = 5.6066(1)$ $c = 7.8918(2)$ $\beta = 90.049(3)$	5.79, 4.50, 1.28	0.97	$La_2Ti_2O_7$, ZnO
	$La_2Ti_2O_7$	3(2)	$Pna2_1$	$a = 25.72(1)$ $b = 7.813(3)$ $c = 5.543(2)$ $V = 1113.9(8)$		1.60	
	ZnO	1.2(1)	$P6_3mc$	$a = 3.2497(5)$ $c = 5.206(1)$ $V = 47.61(2)$		0.72	

the La^{3+} sites. Similarly, it is suggested that the Mn^{4+} ions occupy the (Ti/Mg/Zn) site ($r[Mn^{4+}] = 0.53$ Å, CN = 6; $r[Ti^{4+}] = 0.605$ Å, CN = 6). However, the doped Bi^{3+} and Mn^{4+} contents are too small to give a trace in $LM_{(1-w)}Z_wT$ ($0 \leq w \leq 1$) by the Rietveld refinement. Tables S1 and S2 (ESI†) show the coordinates of the atoms and the main bond lengths, respectively. Surprisingly, the XRD patterns of the samples with $w \geq 0.25$ reveal noticeable peak broadening and a full width at half maximum (FWHM) change at $2\theta = 57.4°$ with a jump from $w = 0$ to $w = 0.25$, as presented in Fig. S2 (ESI†). This obvious jump between $w = 0$ and $w = 0.25$ can be associated with the phase transition from the $Pbnm$ to $P2_1/n$ phases. The cell parameters per the Zn^{2+} concentration w (Fig. 2) also show a jump in the range of $w = 0$–0.25, further proving the existence of the phase transition $Pbnm \leftrightarrow P2_1/n$. According to a previous report, Aguadero et al.[43] proved that there were two Zn^{2+} sites in La_2ZnTiO_6, and that the Ti^{4+}/Zn^{2+} ions were intermixed in the two sites. Meden et al.[41] also showed that the Ti^{4+}/Mg^{2+} ions in

La_2MgTiO_6 are also intermixed. In our case, the Mg^{2+} ions were replaced by the Zn^{2+} ions, and therefore we suggest that Zn/Ti/Mg intermixing occurs.

The occupations, occ(Zn), occ(Ti) and occ(Mg) are refined with linear restrictions, so that the resulting chemical formula remains similar to the suggested one. All of the cell parameters increase with increasing w starting from $w = 0.25$, which is in a good agreement with the larger Zn^{2+} ionic radius compared to the Mg^{2+} ionic radius (Fig. 2). In addition, the average bond length d(Ti/Mg/Zn–O) increases with increasing w (Fig. S3, ESI†), and all these facts prove the reliability of the suggested chemical formulas.

In order to depict the crystal structure transformation process of $LM_{(1-w)}Z_wT:0.005Bi^{3+},0.002Mn^{4+}$ with increasing w values, a schematic structure variation based on the refinement results is shown in Fig. 3. It can be observed that $LMT:0.005Bi^{3+},0.002Mn^{4+}$ and $LZT:0.005Bi^{3+},0.002Mn^{4+}$ are isomorphic, and that both belong to the double perovskite-type
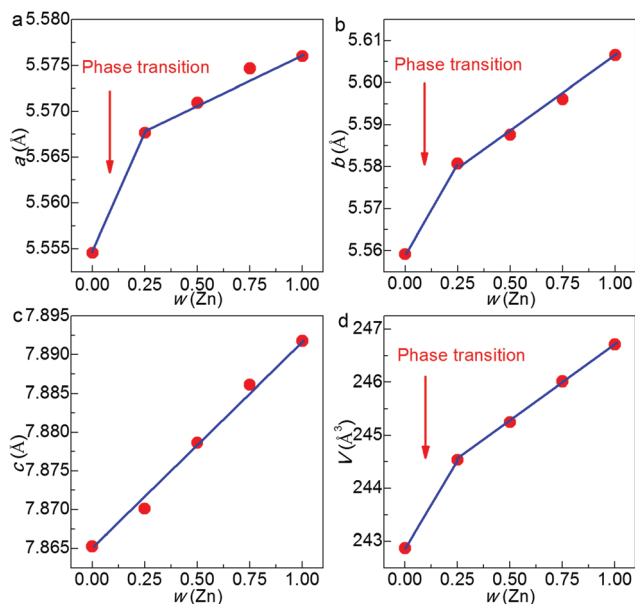
This journal is © The Royal Society of Chemistry 2018

J. Mater. Chem. C, 2018, **6**, 13136–13147 | **13139**

Fig. 2 The cell parameters of the $LM_{(1-w)}Z_wT$:$0.005Bi^{3+}$,$0.002Mn^{4+}$ ($0 \leq w \leq 1$) dependences as per the Zn^{2+} concentration (w): (a) a; (b) b; (c) c; and (d) V. The red arrows represent the probable region of the phase transition between the $Pbnm$ and $P2_1/n$ phases.

$ABB'O_6$ family. The basic three-dimensional framework of $LM_{(1-w)}Z_wT$:$0.005Bi^{3+}$,$0.002Mn^{4+}$ ($0 \leq w \leq 1$) is built by a vertex-sharing $[Ti/Mg/ZnO_6]$ octahedra. Notably, the local symmetry and coordination environment between LMT:$0.005Bi^{3+}$,$0.002Mn^{4+}$ and LZT:$0.005Bi^{3+}$,$0.002Mn^{4+}$ are quite different.

LMT:Bi^{3+},Mn^{4+} belongs to a orthorhombic system (space group $Pbnm$) with unit-cell parameters of $a = 5.5546(2)$ Å, $b = 5.5592(1)$ Å, $c = 7.8652(2)$ Å and $V = 242.87(1)$ Å^3, in which only one type of Mg^{2+}/Ti^{4+} site exists at the 4b (0.5, 0, 0) sites, forming the $[Mg/TiO_6]$ octahedra. The La^{3+} ions are coordinated by 12 adjacent O^{2-} ions, forming a $[LaO_{12}]$ polyhedron with a high 'm' (C_s) symmetry. In contrast the LZT:$0.005Bi^{3+}$,$0.002Mn^{4+}$ is indexed with a monoclinic unit cell (space group $P2_1/n$) with unit-cell parameters of $a = 5.5760(2)$ Å, $b = 5.6066(1)$ Å, $c = 7.8918$ Å and $V = 246.71(1)$ Å^3. Two different Zn^{2+}/Ti^{4+} sites
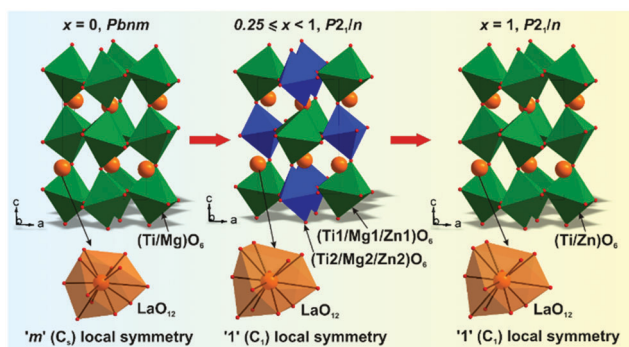
exist, including Zn1/Ti1 (mainly occupied by Zn^{2+}) at the 2c (0, 0.5, 0) sites and Zn2/Ti2 (mainly occupied by Ti^{4+}) at the 2d (0, 0, 0.5) sites. In this case, La^{3+} is also coordinated by 12 adjacent O^{2-} ions forming a $[LaO_{12}]$ polyhedron with the lowest '1' (C_1) symmetry. In view of the appearance of the phase transition from $Pbnm$ to $P2_1/n$ in the $LM_{(1-w)}Z_wT$:$0.005Bi^{3+}$, $0.002Mn^{4+}$ ($0 \leq w \leq 1$) phosphors, two obvious local structure variations can be observed. On the one hand, the (Ti/Mg/Zn) site splits into two lattice sites, marked as the (Ti1/Mg1/Zn1) and (Ti2/Mg2/Zn2) sites, which may exert an influence on the luminescence of Mn^{4+}. On the other hand, the local symmetry of the $[LaO_{12}]$ polyhedron decreases from the 'm' (C_s) symmetry to the lowest '1' (C_1) symmetry. The variation of the local coordination environment of the (Ti/Mg/Zn) site and the symmetry of the $[LaO_{12}]$ polyhedron are suggested to influence the luminescence of the Bi^{3+} and Mn^{4+} in the $LM_{(1-w)}Z_wT$:$0.005Bi^{3+}$,$0.002Mn^{4+}$ ($0 \leq w \leq 1$) phosphors.

Fig. 4a shows the SEM image of the representative $LM_{0.5}Z_{0.5}T$:$0.005Bi^{3+}$,$0.002Mn^{4+}$ sample. It can be observed that the as-prepared sample is assembled by irregular particles that are about 0.2–0.5 μm in diameter. The elemental analysis is revealed via the SEM mapping images of $LM_{0.5}Z_{0.5}T$:$0.005Bi^{3+}$, $0.002Mn^{4+}$ in Fig. 4b–h. Evidently, the studied sample contains La, Mg, Zn, Ti, O, Bi and Mn, and they are uniformly distributed throughout the whole viewing area. In addition, the peaks for the La, Mg, Zn, Ti, O, Bi and Mn elements appear in the EDS spectrum (Fig. 4i), indicating that the Bi^{3+} ions and Mn^{4+} ions are successfully doped into the $LM_{0.5}Z_{0.5}T$ solid solution. On the basis of the EDS results, the atomic ratio of La, Mg, Zn, Ti, and O is calculated to be 3.94 : 1.06 : 1 : 1.93 : 13.72, which is very close to the theoretical atomic ratio in $LM_{0.5}Z_{0.5}T$:$0.005Bi^{3+}$, $0.002Mn^{4+}$. These results demonstrate the successful synthesis of the designed $LM_{(1-w)}Z_wT$:$0.005Bi^{3+}$,$0.002Mn^{4+}$ ($0 \leq w \leq 1$)

Fig. 3 The crystal structure transformation process of $LM_{(1-w)}Z_wT$: $0.005Bi^{3+}$,$0.002Mn^{4+}$ ($0 \leq w \leq 1$) by phase transition. The main feature is a single (Ti/Mg/Zn) site splitting into two (Ti1/Mg1/Zn1), (Ti2/Mg2/Zn2) sites, and the decreasing local symmetry of the $[LaO_{12}]$ polyhedron.
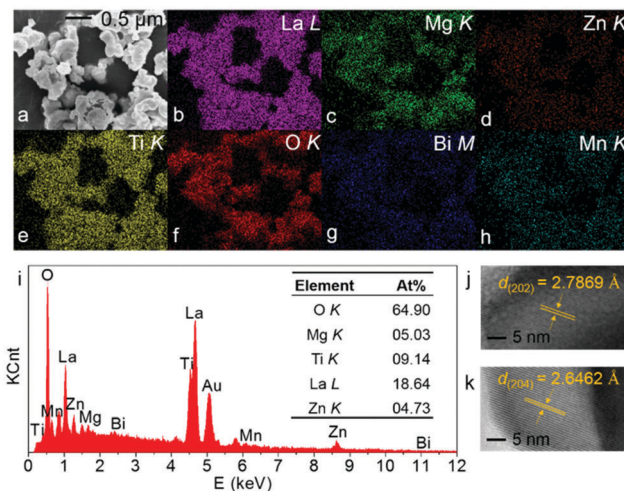

Fig. 4 (a) SEM images of the representative $LM_{0.5}Z_{0.5}T$:$0.005Bi^{3+}$, $0.002Mn^{4+}$ sample. (b–h) The corresponding elemental mapping analysis for the La, Mg, Zn, Ti, O, Bi and Mn elements in $LM_{0.5}Z_{0.5}T$:$0.005Bi^{3+}$, $0.002Mn^{4+}$. (i) The EDS spectra of $LM_{0.5}Z_{0.5}T$:$0.005Bi^{3+}$,$0.002Mn^{4+}$, the inset is the atom percentage in $LM_{0.5}Z_{0.5}T$:$0.005Bi^{3+}$,$0.002Mn^{4+}$. HRTEM images of (j) LMT:$0.005Bi^{3+}$,$0.002Mn^{4+}$ and (k) LZT:$0.005Bi^{3+}$,$0.002Mn^{4+}$.

samples. Moreover, the HRTEM images of the representative LMT:0.005Bi^{3+},0.002Mn^{4+} and LZT:0.005Bi^{3+},0.002Mn^{4+} samples present clear lattice fringes (Fig. 4j–k), demonstrating a good crystallinity. The d-spacing of LMT:0.005Bi^{3+},0.002Mn^{4+} is 2.7869 Å, corresponding to a (202) plane, and for LZT:0.005Bi^{3+},0.002Mn^{4+} it is 2.6462 Å, corresponding to a (204) plane, respectively.

Given the sensitivity of Bi^{3+} ions to the coordination environment, the optical properties of the LM$_{(1-w)}$Z$_w$T:0.005Bi^{3+}, 0.002Mn^{4+} ($0 \leq w \leq 1$) samples with varying w values are discussed in detail. The optical indirect band gaps of the LMT and LZT hosts were first calculated using the following formula based on the diffuse reflection spectra:[44–46]

$$[F(R)h\nu]^{1/2} = A(h\nu - E_g)$$

$$F(R) = (1 - R)^2/2R \qquad (1)$$

In which A stands for the absorption constant, E_g represents the optical band gap, $h\nu$ is the photon energy, $F(R)$ is the absorption coefficient, and R is the reflectance (%) coefficient, respectively. Fig. 5a depicts the plots of $[F(R)h\nu]^{1/2}$ *versus* the $h\nu$ of the LMT and LZT host. The calculated E_g values for the LMT and LZT host are 3.95 eV and 3.84 eV respectively, indicating that both of the LMT and LZT are suitable hosts for Bi^{3+} and Mn^{4+}-doping. To detect the photoluminescence absorption properties of the Bi^{3+}, Mn^{4+} co-doped LM$_{(1-w)}$Z$_w$T phosphors, the UV-vis DRS for different Zn^{2+} concentration samples ($w = 0, 0.5, 1$) are collected and shown in Fig. 5b, which mainly includes four absorption bands. The first absorption band located at about 330 nm is ascribed to the Mn–O charge transfer band (CTB). The second absorption band arises from the $^1S_0 \rightarrow \ ^1P_1/^3P_1$ transition of the Bi^{3+} with the center at around 350 nm. The transitions of $^4A_2 \rightarrow \ ^4T_1$ and $^4A_2 \rightarrow \ ^2T_2$ of Mn^{4+} contribute to the third absorption band, which is from 355 nm to 475 nm. Finally, the forth absorption band from 450 nm to 600 nm with the maximum at around 500 nm originates from the $^4A_2 \rightarrow \ ^4T_2$ transitions of the Mn^{4+}.

To study the effect of the phase transition and Zn$^{2+} \rightarrow$ Mg^{2+} substitution on the photoluminescence properties of LM$_{(1-w)}$T$_w$:0.005Bi^{3+},0.002Mn^{4+} ($0 \leq w \leq 1$), their PLE and PL spectra were recorded and analyzed. Fig. S4 (ESI†) and Fig. 5c show the normalized PLE spectra of LM$_{(1-w)}$T$_w$:0.005Bi^{3+},0.002Mn^{4+} ($w = 0$–1) monitored at 420 nm for Bi^{3+} and 710 nm for Mn^{4+}, respectively. When monitored at 420 nm, the PLE spectra of Bi^{3+} possesses an absorption broad band from 275 nm to 375 nm with the maximum located at 345 nm, attributed to the $^1S_0 \rightarrow \ ^1P_1/^3P_1$ transitions of Bi^{3+}. When monitored at 710 nm, all of the PLE spectra of the $w = 0$–1.0 samples include two evidently broad absorption bands in the region of 275–550 nm. The stronger absorption band is from 275 nm to 450 nm with the maximum at 340–395 nm, while the weaker one is from 450 nm to 550 nm and centered at 500 nm. Based on the Gaussian fitting function, the PLE spectra could be divided into four characteristic peaks, which originate from the CTB of Mn–O and the electron transition of $^4A_{2g} \rightarrow \ ^4T_{1g}$, $^4A_{2g} \rightarrow \ ^2T_{2g}$, $^4A_{2g} \rightarrow \ ^4T_{2g}$ for Mn^{4+} (Fig. S5a and b, ESI†). The Gaussian deconvoluted peaks of LMT:0.005Bi^{3+},0.002Mn^{4+} are located at 325, 357, 388 and
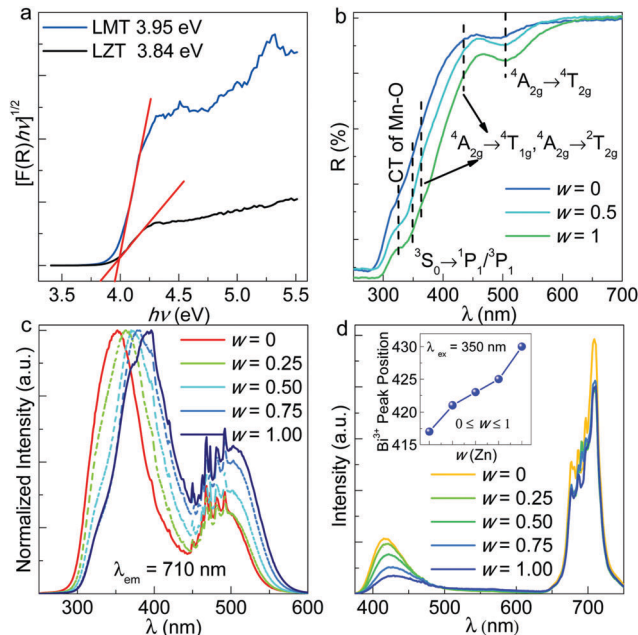

Fig. 5 (a) The relationship of the $[F(R)h\nu]^{1/2}$ *vs.* the photon energy $h\nu$ in the LMT and LZT host. (b) DRS corresponding to LM$_{(1-w)}$Z$_w$T:0.005Bi^{3+}, 0.002Mn^{4+} ($w = 0, 0.5,$ and 1). (c) Normalized PLE spectra of the Mn^{4+} ions in LM$_{(1-w)}$Z$_w$T:0.005Bi^{3+},0.002Mn^{4+} ($w = 0, 0.25, 0.50, 0.75,$ and 1). (d) PE spectra of LM$_{(1-w)}$Z$_w$T:0.005Bi^{3+},0.002Mn^{4+} ($w = 0, 0.25, 0.50,$ 0.75, and 1), the inset is the Bi^{3+} peak position as a function of the Zn^{2+} concentration.

484 nm, respectively. For LZT:0.005Bi^{3+},0.002Mn^{4+}, the Gaussian deconvoluted peaks are located at 338, 386, 478 and 520 nm. These results are consistent with the diffusion reflection spectra discussed previously.

Obviously, a red shift appears in the Mn^{4+} PLE spectra as the w value increases. We speculate that the variation in the [Ti/Mg/ZnO$_6$] octahedra coordination environment is the primary reason for this. Owing to the special 3d^3 electron configuration, the electron transition of the Mn^{4+} energy levels is easily influenced by the crystal field (CF) environment. When $w \geq 0.25$, a phase transition exists in LM$_{(1-w)}$Z$_w$T:0.005Bi^{3+}, 0.002Mn^{4+} ($0 \leq w \leq 1$), caused by Zn/Mg/Ti splitting into two different sites. Thereafter, the CF symmetry of the [Ti/Mg/ZnO$_6$] octahedra decreases, which is influenced by the larger distortion with an increasing Zn^{2+} concentration (Fig. S6, ESI†).[47,48] As the CF environment varies, the Mn^{4+} excited state levels, $^4T_{1g}$, $^2T_{2g}$ and $^4T_{2g}$, change accordingly,[49] resulting in a PLE spectra red shift of the Mn^{4+} ions in LM$_{(1-w)}$Z$_w$T:0.005Bi^{3+},0.002Mn^{4+} ($0 \leq w \leq 1$).

Upon excitation at 345 nm n-UV light, the PL spectra of the LM$_{(1-w)}$Z$_w$T:0.005Bi^{3+},0.002Mn^{4+} samples simultaneously present the characteristic emissions for the Bi^{3+} and Mn^{4+} ions with the emission peaks at 420 nm and 710 nm, respectively, as shown in Fig. 5d. According to the discussion above, the larger Zn^{2+} ions occupy the Zn/Mg/Ti sites, and the average bond length of the Zn/Mg/Ti–O gradually elongate (Fig. S3, ESI†), resulting in the expansion of the [Zn/Mg/TiO$_6$] octahedra. Consequently, the [LaO$_{12}$] polyhedra will be squeezed by the

This journal is © The Royal Society of Chemistry 2018

J. Mater. Chem. C, 2018, **6**, 13136–13147 | **13141**

adjacent $[Zn/Mg/TiO_6]$ octahedra, which leads to a decreasing symmetry of the $[LaO_{12}]$ polyhedron from the 'm' (C_s) symmetry to the '1' (C_1) symmetry with the increasing w (Fig. 3). Finally, this generates a red-shift in the PL spectra of Bi^{3+} from 417 to 428 nm (see inset of Fig. 5d). However, the CF strength seldomly influences the excited state level, ^2E_g, of Mn^{4+}.[50] Hence, the red emission peaks of the Mn^{4+} ions ($^2E_g \rightarrow {^4A_{2g}}$ transitions) are basically located at 710 nm with the increasing Zn^{2+} concentration.

3.2 Energy transfer from Bi^{3+} to Mn^{4+}

Efficient energy transfer could not only vastly improve the luminescence efficiency of activators, but could also realize the controllable luminescence tuning of the characteristic emission from the sensitizers to activators.[51] These changes could help optimize various luminescence performances of phosphors to promote their application in pc-WLEDs. According to the structural discussions detailed above, the Bi^{3+} and Mn^{4+} ions are suggested to preferentially occupy the La^{3+} and Ti^{4+} sites in the LMT and LZT systems, respectively. However, a small quantity of Mn^{4+} ions could possibly enter into the Mg^{2+} or Zn^{2+} sites, owing to the same site-occupation of the Mg^{2+}/Zn^{2+} and Ti^{4+} (Table S1, ESI,† $w = 0$ and $w = 1$). In order to enhance the red emission of the Mn^{4+} ions, we designed the $Bi^{3+} \rightarrow Mn^{4+}$ energy transfer in the LMT and LZT series. A series of Bi^{3+}-doped, Mn^{4+}-doped and Bi^{3+}/Mn^{4+} co-doped LMT and LZT phosphors were successfully synthesized.

Fig. S7 (ESI†) and Fig. 6 show the XRD spectra of the as-prepared powders, all of the XRD diffraction peaks of the as-prepared samples are in good agreement with the standard LMT (ICSD No. 86852) and LZT (ICSD No. 174571), respectively, without any apparent impurities. These results prove that all of the as-prepared samples are pure phases.

Fig. 7a shows the PLE and PL spectra for LMT:$0.005Bi^{3+}$ and LMT:$0.002Mn^{4+}$, meanwhile the PLE and PL spectra of $L_{(1-u)}MT{:}uBi^{3+}$ ($0 \leq u \leq 0.03$) and LMT$_{(1-z)}{:}zMn^{4+}$ ($0 \leq z \leq 0.01$) are shown in Fig. S8 and S9 (ESI†), respectively. For the LMT:$0.005Bi^{3+}$, there is an obvious absorption band from 275 to 375 nm centered at 340 nm, which is ascribed to the $^1S_0 \rightarrow {^1P_1}$ and $^1S_0 \rightarrow {^3P_1}$ transitions of Bi^{3+}. When monitoring at 340 nm,
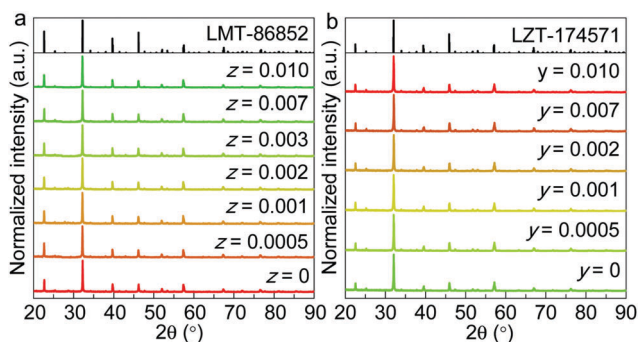
Fig. 7 (a) The PLE and PL spectra of LMT:$0.005Bi^{3+}$ (blue) and LMT:$0.002Mn^{4+}$ (cyan). (b) The PL spectra of LMT$_{(1-z)}$:$0.005Bi^{3+}$,zMn^{4+} ($0 \leq z \leq 0.01$). The inset shows the integrated intensity of the Bi^{3+} and Mn^{4+} emission as a function of the Mn^{4+} concentrations (z). (c) The CIE chromaticity coordinate diagram for LMT$_{(1-z)}$:$0.005Bi^{3+}$,zMn^{4+} ($0 \leq z \leq 0.01$), the insets show luminescence photographs of LMT:$0.005Bi^{3+}$ and LMT:$0.005Bi^{3+}$,$0.010Mn^{4+}$, respectively, under 365 nm n-UV excitation. (d) The energy transfer efficiency (η_T) of LMT$_{(1-z)}$:$0.005Bi^{3+}$,zMn^{4+} ($0 \leq z \leq 0.01$) as a function of the Mn^{4+} concentration (z). (e) Photoluminescence decay curves of the Bi^{3+} emission detected at 370 nm for LMT:$0.005Bi^{3+}$,zMn^{4+} ($0 \leq z \leq 0.01$). (f) The decay lifetime of LMT$_{(1-z)}$:$0.005Bi^{3+}$,zMn^{4+} ($0 \leq z \leq 0.01$) as a function of the Mn^{4+} concentration (z).

a blue emission (375–500 nm) with a maximum at 417 nm of Bi^{3+} is detected, originating from the $^3P_1 \rightarrow {^1S_0}$ transitions. When the Mn^{4+} ions enter into the LMT host, a strong red emission band from 650 to 750 nm with an emission peak at 710 nm is observed owing to the Mn^{4+}:^2E_g–$^4A_{2g}$ transitions. Apparently, there is spectral overlap from 455 to 490 nm between the emission spectrum of Bi^{3+} and the excitation spectra of Mn^{4+}. Simultaneously, a co-excitation band from 300 to 375 nm exists in the LMT:$0.005Bi^{3+}$ and LMT:$0.002Mn^{4+}$ samples. Hence, there is a good possibility of an energy transfer between the Bi^{3+} and Mn^{4+} in LMT. To verify the $Bi^{3+} \rightarrow Mn^{4+}$ energy transfer in the LMT host, a range of PL spectra for the LMT$_{(1-z)}$:$0.005Bi^{3+}$,zMn^{4+} ($0 \leq z \leq 0.01$) samples under a 340 nm wavelength were collected and are shown in Fig. 7b. It was found that both the blue emission from Bi^{3+} and the red emission from Mn^{4+} appear in all of the Bi^{3+}/Mn^{4+} co-doped samples. When mixing the Bi^{3+}-doping concentration in the

Fig. 6 XRD patterns of (a) the LMT$_{(1-z)}$:$0.005Bi^{3+}$,zMn^{4+} ($0 \leq z \leq 0.01$) samples and (b) the LZT$_{(1-y)}$:$0.005Bi^{3+}$,yMn^{4+} ($0 \leq y \leq 0.01$) samples. The standard XRD data for LMT (ICSD No. 86852) and LZT (ICSD No. 174571) are shown as references.
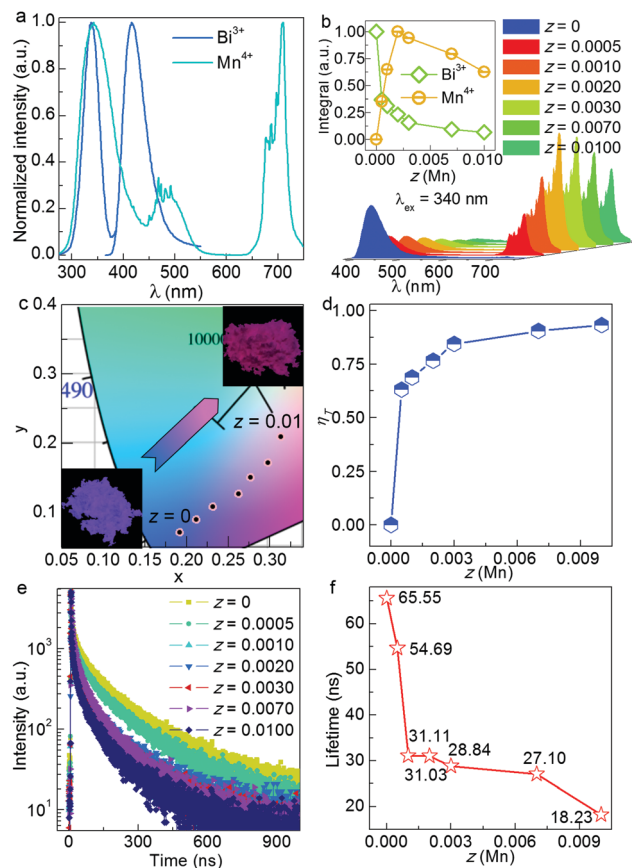
13142 | *J. Mater. Chem. C*, 2018, **6**, 13136–13147

This journal is © The Royal Society of Chemistry 2018

Table 2 CIE color coordinates of $LMT_{(1-z)}$:0.005Bi^{3+},$z$$Mn^{4+}$ ($0 \leq z \leq$ 0.01) and $LZT_{(1-y)}$:0.005Bi^{3+},$y$$Mn^{4+}$ ($0 \leq y \leq$ 0.01)

Sample	$z/y$$Mn^{4+}$	x	y
$LMT_{(1-z)}$:0.005Bi^{3+},$z$$Mn^{4+}$ ($0 \leq z \leq$ 0.01)			
1	0	0.173	0.069
2	0.0005	0.197	0.088
3	0.001	0.221	0.106
4	0.002	0.258	0.126
5	0.003	0.277	0.149
6	0.007	0.312	0.175
7	0.010	0.320	0.209
$LZT_{(1-y)}$:0.005Bi^{3+},$y$$Mn^{4+}$ ($0 \leq y \leq$ 0.01)			
1	0	0.214	0.172
2	0.0005	0.279	0.224
3	0.001	0.285	0.209
4	0.002	0.398	0.244
5	0.007	0.406	0.239
6	0.010	0.418	0.247

$LMT_{(1-z)}$:0.005Bi^{3+},$z$$Mn^{4+}$ system, the emission intensity of Bi^{3+} gradually decreases with the increase of the Mn^{4+}-doping concentration. In contrast, the emission intensity of Mn^{4+} presents a monotonous increase before $z = 0.002$, as shown in the inset of Fig. 7b. These results also indicate that there is an energy transfer in the LMT:Bi^{3+}/Mn^{4+} co-doped phosphors. Beyond $z = 0.002$, concentration quenching of the Mn^{4+} emission occurs. This is because the distance to the adjacent Mn^{4+} becomes shorter with an increase in the doping concentration, and then the Mn^{4+}–Mn^{4+} interaction strengthens, resulting in the luminescence quenching of Mn^{4+} in the LMT:Bi^{3+}/Mn^{4+} co-doped system.

Fig. 7c and Table 2 show that the CIE chromaticity coordinates of $LMT_{(1-z)}$:0.005Bi^{3+},$z$$Mn^{4+}$ ($0 \leq z \leq$ 0.01) vary from (0.1729, 0.0689) to (0.3202, 0.2086) with the increasing z values, and thus the emission colors could be adjusted from the blue to the pink region. The corresponding luminescence photos of the $z = 0$ and $z = 0.01$ samples also demonstrate the color tuning from blue to pink light, further confirming the existence of the $Bi^{3+} \rightarrow Mn^{4+}$ energy transfer. The energy transfer efficiency of $LMT_{(1-z)}$:0.005Bi^{3+},$z$$Mn^{4+}$ ($0 \leq z \leq$ 0.01) can be determined using the following equation:[52]

$$\eta_T = 1 - \frac{I_S}{I_{S_0}} \qquad (2)$$

in which η_T stands for the energy transfer efficiency, and I_S and I_{S_0} represent the emission intensity with and without the Mn^{4+} ions respectively. The calculated η_T for $LMT_{(1-z)}$:0.005Bi^{3+},$z$$Mn^{4+}$ ($0 \leq z \leq$ 0.01) are shown in Fig. 7d, which are 63%, 68%, 76%, 84%, 90% and 93% for $z = 0.0005$, 0.001, 0.002, 0.003, 0.007 and 0.010, respectively. This result proves the existence of the highly efficient $Bi^{3+} \rightarrow Mn^{4+}$ energy transfer in the $LMT_{(1-z)}$:0.005Bi^{3+}, $z$$Mn^{4+}$ ($0 \leq z \leq$ 0.01) phosphors.

To better understand luminescence dynamics that occur during the energy transfer of the $LMT_{(1-z)}$:0.005Bi^{3+},$z$$Mn^{4+}$ ($0 \leq z \leq$ 0.01), the photoluminescence decay curves and calculated lifetime values of Bi^{3+} for various Mn^{4+} concentrations are measured and depicted in Fig. 7e and f, respectively. Under 370 nm n-UV light excitation, the decay lifetimes for the

Bi^{3+} emission of the $LMT_{(1-z)}$:0.005Bi^{3+},$z$$Mn^{4+}$ ($0 \leq z \leq$ 0.01) samples are determined using the following equation:

$$I_T = I_0 \exp\left(\frac{-t}{\tau}\right) \qquad (3)$$

in which I_0 and I_t represent the luminescence intensities of Bi^{3+} at t_0 and t, and τ represents the luminescence decay lifetimes for the corresponding samples. With the increase in the Mn^{4+} concentration, the decay lifetimes are calculated to be 65.55, 54.69, 31.11, 31.03, 28.84, 27.10, and 18.23 ns, respectively. Obviously, the lifetimes of Bi^{3+} present a monotonous decrease with increasing z values, which provides favorable evidence to confirm the existence of the $Bi^{3+} \rightarrow Mn^{4+}$ energy transfer.

Normally, the energy transfer process mainly originates from two kinds of interaction: one is the exchange interaction and the other is a multipolar interaction, these are determined based on the critical distance (R_c). R_c is the distance between the sensitizers and activators. It is known that if the distance between the sensitizers and activators is shorter than 4 Å, an exchange interaction will occur. If the distance is located between 4 Å and 27 Å, a multipolar interaction will occur. The R_c is usually judged using following equation:[53,54]

$$R_c \approx 2\left(\frac{3V}{4\pi x_c N}\right)^{1/3} \qquad (4)$$

In which V is the volume of the unit cell, x_c is the sum concentration of the Bi^{3+} and Mn^{4+} ions, and N is the number of cations in the unit cell. In the $LMT_{(1-z)}$:0.005Bi^{3+},$z$$Mn^{4+}$ ($0 \leq z \leq$ 0.01) series, V is 242.87 Å³, x_c is 0.007, and N is 4, respectively. Consequently, the calculated R_c is 25.49 Å. When energy transfer occurs from the Bi^{3+} ions to the Mn^{4+} ions the in LMT host, the multipolar interaction plays a major role.

As there is a similarity between the crystal structure of LMT and LZT, the $Bi^{3+} \rightarrow Mn^{4+}$ energy transfer could also be expected to occur in the LZT host. Fig. 8a shows the PLE and PL spectra of LZT:0.005Bi^{3+} and LZT:0.002Mn^{4+}. When the Bi^{3+} ions are incorporated into the LZT host, a broad absorption from 275 to 375 nm centered at 355 nm is observed owing to the $^1S_0 \rightarrow {}^1P_1/{}^3P_1$ transitions of Bi^{3+}. Under excitation at a wavelength of 355 nm, the emission spectra of LZT:0.005Bi^{3+} includes two emission bands from 375 to 650 nm with two emission centers at 428 nm and 550 nm, respectively. This phenomenon exists throughout the whole $L_{(1-x)}$ZT:$x$$Bi^{3+}$ series (Fig. S10, ESI†). Nevertheless, on the basis of the previous Rietveld refinement result shown in Table S1 (ESI†) ($w = 1$), there is only one site for the La^{3+} ions in the LZT. Hence, we speculated that a small number of Bi^{3+} ions could possibly occupy the interstitial lattice position of LZT, generating the 550 nm emission. When the Mn^{4+} ions enter into the LZT host (Fig. S11, ESI†), the resulting PLE and PL spectra are almost the same as that of LMT:Mn^{4+}. Notably, a wide spectral overlap between the emission spectra of Bi^{3+} and the excitation spectra of Mn^{4+} is observed in Fig. 8a. This indicates that an energy transfer may occur between the Bi^{3+} ions and the Mn^{4+} ions in $LZT_{(1-y)}$:0.005Bi^{3+},$y$$Mn^{4+}$ ($0 \leq y \leq$ 0.01). When the Bi^{3+} concentrations are fixed and the Mn^{4+}-doping concentrations are

This journal is © The Royal Society of Chemistry 2018

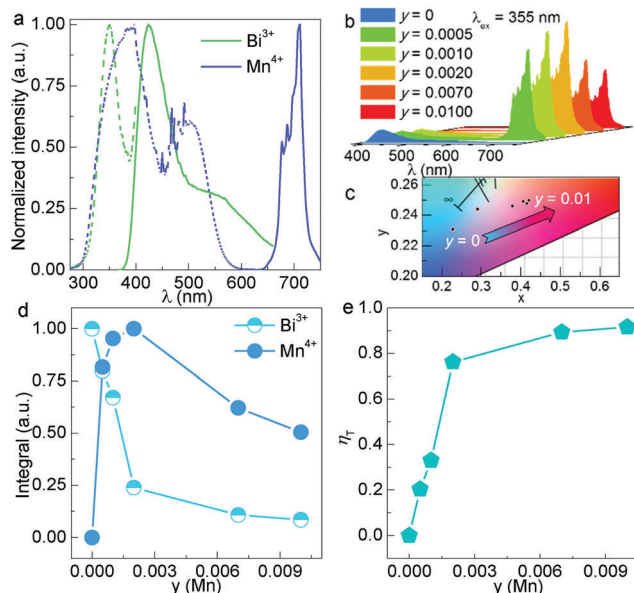*J. Mater. Chem. C*, 2018, **6**, 13136–13147 | **13143**

Fig. 8 (a) The PLE and PL spectra of LZT:0.005Bi^{3+} (green) and LZT:0.002Mn^{4+} (navy blue). (b) The PL spectra; and (c) CIE chromaticity coordinates diagram for LZT$_{(1−y)}$:0.005Bi^{3+},yMn^{4+} ($0 \leq y \leq 0.01$). (d) Integrated intensity of the Bi^{3+} and Mn^{4+} emission as a function of the Mn^{4+}-doping concentrations (y). (e) The energy transfer efficiency of LZT$_{(1−y)}$:0.005Bi^{3+},yMn^{4+} ($0 \leq y \leq 0.01$) as a function of the Mn^{4+}-doping concentrations (y).

changed, it is found that the Bi^{3+} blue emission gradually decreases while the Mn^{4+} red emission simultaneously increases under $y = 0.002$ in the Bi^{3+}/Mn^{4+} co-doped LZT samples (Fig. 8b and d). The reduced emission intensity for Mn^{4+} ions beyond $y = 0.002$ could also be attributed to the concentration quenching effect. Meanwhile, the CIE chromaticity diagram in Fig. 8c reveals that the color coordinates of LZT$_{(1−y)}$:0.005Bi^{3+},yMn^{4+} ($0 \leq y \leq 0.01$) gradually shift from (0.2142, 0.1716) to (0.4117, 0.2465) with increasing Mn^{4+} concentrations, implying a broad color tuning from blue to red light. The detailed CIE color coordinate values of the LZT$_{(1−y)}$:0.005Bi^{3+},yMn^{4+} ($0 \leq y \leq 0.01$) samples calculated via the PL spectra are summarized in Table 2. The above results further confirm the appearance of the Bi$^{3+} \rightarrow$ Mn^{4+} energy transfer in the LZT host. The Bi$^{3+} \rightarrow$ Mn^{4+} energy transfer efficiency in LZT$_{(1−y)}$:0.005Bi^{3+},yMn^{4+} ($0 \leq y \leq 0.01$) are similarly calculated using formula 1 (Fig. 8e). The η_T values of LZT$_{(1−y)}$:0.005Bi^{3+},yMn^{4+} ($0 \leq y \leq 0.01$) are 20%, 32%, 76%, 89%, 91% for $y = 0.0005$, 0.001, 0.002 0.007, 0.01, respectively, revealing the effective energy transfer in LZT$_{(1−y)}$:0.005Bi^{3+},yMn^{4+}. In addition, the R_c between the Bi^{3+} and Mn^{4+} in the LZT$_{(1−y)}$:0.005Bi^{3+},yMn^{4+} ($0 \leq y \leq 0.01$) was calculated to be 25.28 Å, which is also ascribed to the electric multipolar interaction.

The specific type of electric multipolar interaction between the Bi^{3+} and Mn^{4+} in LAT$_{(1−y)}$:0.005Bi^{3+},yMn^{4+} (A = Mg, Zn) ($0 \leq y \leq 0.01$) systems can be determined using Dexter's formula:[55–57]

$$\frac{\eta_{S_0}}{\eta_S} \propto C^{n/3} \tag{5}$$

In which η_{S_0}/η_S represents the ratio of the quantum efficiency without and with the Bi^{3+}-doped samples. C represents the total concentration of the Bi^{3+} and Mn^{4+} ions. n is a constant which influences the interaction relationship of Bi^{3+} and Mn^{4+}, when $n = 6$, 8, and 10, this corresponds with dipole–dipole, dipole–quadrupole and quadrupole–quadrupole interactions, respectively. The value of η_{S_0}/η_S can be approximately replaced by the ratio of the emission intensity of I_{S_0}/I_S. Hence, the following formula can be expressed as follows:

$$\frac{I_{S_0}}{I_S} \propto C^{n/3} \tag{6}$$

In which I_{S_0} represents the initial emission intensity of Bi^{3+}, and I_S represents the emission intensity of the Bi^{3+}/Mn^{4+} co-doped phosphors when $n = 6$, 8, 10. The relationship between the I_{S_0}/I_S and $C^{n/3}$ of LMT$_{(1−z)}$:0.005Bi^{3+},zMn^{4+} ($0 \leq z \leq 0.01$) and LZT$_{(1−y)}$:0.005Bi^{3+},yMn^{4+} ($0 \leq y \leq 0.01$) is shown in Fig. 9a–c and d–f, respectively. The maximal correlation coefficient of the linear fitting can be achieved at $n = 6$ for both of the above two series, indicating that the dipole–dipole interaction contributes to the energy transfer between the Bi^{3+} and Mn^{4+} in the LAT$_{(1−y)}$:0.005Bi^{3+},yMn^{4+} (A = Mg, Zn) ($0 \leq y \leq 0.01$) samples.

According to the previous experimental results and analysis, a schematic energy level diagram for the electronic transitions and the energy transfer process in the Bi^{3+}/Mn^{4+} co-doped LAT$_{(1−y)}$:0.005Bi^{3+},yMn^{4+} (A = Mg, Zn) ($0 \leq y \leq 0.01$) phosphors is depicted in Fig. 10. Upon excitation with a 340 or 355 nm n-UV light, the electrons in the Bi^{3+} ions are excited from the
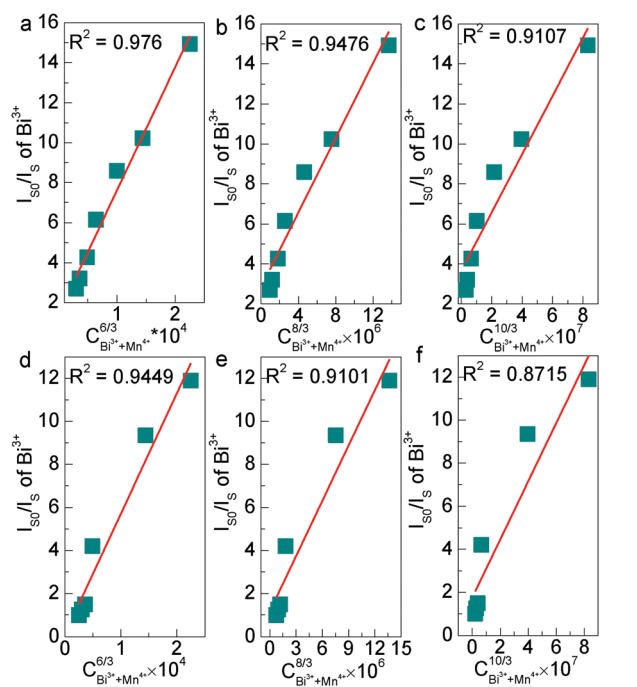

Fig. 9 Dependence of I_{S_0}/I_S of Bi^{3+} ions on (a) $C_{(Bi^{3+}+Mn^{4+})}^{6/3}$; (b) $C_{(Bi^{3+}+Mn^{4+})}^{8/3}$; and (c) $C_{(Bi^{3+}+Mn^{4+})}^{10/3}$ for LMT$_{(1−z)}$:0.005Bi^{3+},zMn^{4+} ($0 \leq z \leq 0.01$). Dependence of I_{S_0}/I_S of Bi^{3+} ions on (d) $C_{(Bi^{3+}+Mn^{4+})}^{6/3}$; (e) $C_{(Bi^{3+}+Mn^{4+})}^{8/3}$; and (f) $C_{(Bi^{3+}+Mn^{4+})}^{10/3}$ for LZT$_{(1−y)}$:0.005Bi^{3+},yMn^{4+} ($0 \leq y \leq 0.01$).

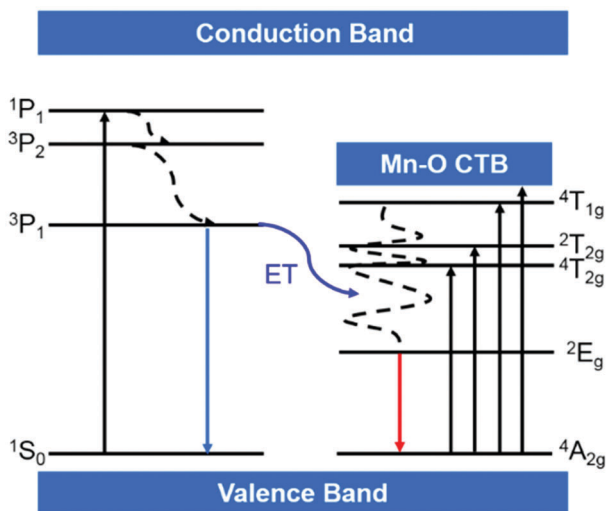**Fig. 10** A schematic energy level diagram for the electronic transitions and the energy transfer processes in the LAT$_{(1-y)}$:0.005Bi^{3+},yMn^{4+} (A = Mg, Zn) (0 ≤ y ≤ 0.01) systems.

ground state $^1S_0$ to the excited state $^3P_1$, $^3P_2$, $^1P_1$. Then, a portion of the electrons relax from the $^3P_2$ and $^1P_1$ energy level to the $^3P_1$ energy level and return to the ground state $^1S_0$ energy level, generating a blue emission (417 or 428 nm). Meanwhile, the other electrons located in the excited state level $^3P_1$ transfer their energy to the excited state $^4T_{2g}$ energy level of the neighboring Mn^{4+} ions. In addition, the Mn^{4+} ions can also be excited from the $^4A_{2g}$ to the $^4T_{2g}$, $^2T_{2g}$, and $^4T_{1g}$ energy levels. After the excited electrons in the Mn^{4+} ions relax to the ^2E_g energy level and then return to the $^4A_{2g}$ energy level, this is accompanied by a far-red light emission centered at 710 nm. By designing the energy transfer from the Bi^{3+} to Mn^{4+}, the far-red emission efficiency of the Mn^{4+} ions in the LMT and LZT systems can be markedly improved. The internal quantum efficiency (IQE) values increase from 31.5% (LMT:0.002Mn^{4+}) to 59.5% (LMT:0.005Bi^{3+},0.002Mn^{4+}) and from 40.3% (LZT:0.002Mn^{4+}) to 70.8% (LZT:0.005Bi^{3+},0.002Mn^{4+}) in the LMT and LZT systems, respectively.

3.3 Thermal stability

In practice, the working temperature of pc-WLEDs can reach 150 °C, which will greatly influence the emission intensity, luminescence lifetime and chromaticity of the phosphors.[58–60] Hence, thermal stability is a very important index for phosphors to determine their suitability for practical application in the pc-WLEDs lighting area. In this regard, the thermal stability of LMT$_{(1-z)}$:0.005Bi^{3+},zMn^{4+} (0 ≤ z ≤ 0.01), LZT$_{(1-y)}$:0.005Bi^{3+}, yMn^{4+} (0 ≤ y ≤ 0.01) and LM$_{(1-w)}$Z$_w$T:0.005Bi^{3+},0.002Mn^{4+} (0 ≤ w ≤ 0.01) were detected from 25 to 250 °C using temperature-dependent PL spectra (Fig. 11). The PL intensity of all of the studied samples gradually decreases with the increasing temperature, which could be attributed to the thermal quenching effect induced by the non-radiation transition process. However, as the Mn^{4+} and Mg^{2+}-doped concentration increased, the corresponding emission intensities were all
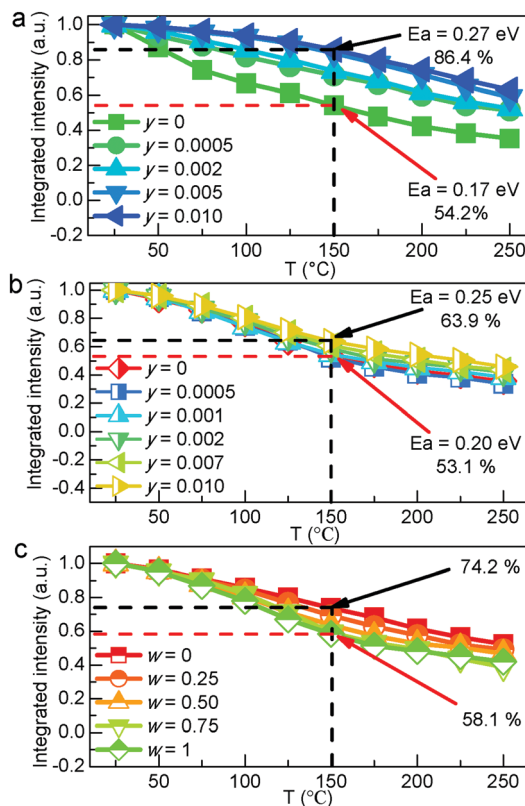

Fig. 11 Temperature-dependent integrated emission spectra of (a) LMT$_{(1-z)}$:0.005Bi^{3+},zMn^{4+} (0 ≤ z ≤ 0.01); (b) LZT$_{(1-y)}$:0.005Bi^{3+},yMn^{4+} (0 ≤ y ≤ 0.01); and (c) LM$_{(1-w)}$Z$_w$T:0.005Bi^{3+},0.002Mn^{4+} (0 ≤ w ≤ 1) excited under 350 nm n-UV light.

enhanced. For the LMT$_{(1-z)}$:0.005Bi^{3+},zMn^{4+} (0 ≤ z ≤ 0.01), LZT$_{(1-y)}$:0.005Bi^{3+},yMn^{4+} (0 ≤ y ≤ 0.01) phosphors, at 150 °C, when the Mn^{4+} concentration varied from 0 to 0.01, the emission intensity at 150 °C of LMT$_{(1-z)}$:0.005Bi^{3+},zMn^{4+} (0 ≤ z ≤ 0.01) increased from 0.54 to 0.86 of the initial intensity at 25 °C. For LZT$_{(1-y)}$:0.005Bi^{3+},yMn^{4+} (0 ≤ y ≤ 0.01), the emission intensity at 150 °C increased from 0.53 to 0.64 of the initial intensity at 25 °C. The increase in the temperature-dependent PL intensity may be related to the non-radiative transition process, which can be represented using the thermal activation energy ΔE_a. The ΔE_a can be obtained using the following formula:

$$I(T) = \frac{I_0}{1 + C \exp(-\Delta E_a/kT)} \qquad (7)$$

In which I_0 is integrated emission intensity at 25 °C and $I(T)$ is integrated emission intensity at temperature T, k is the Boltzmann constant ($k = 8.62 \times 10^{-5}$ eV), and ΔE_a is the thermal activation energy. Then, ΔE_a can be calculated by plotting $\ln[(I_0/I_T) - 1]$ against $10\,000/T$. The calculated ΔE_a values of LMT$_{(1-z)}$:0.005Bi^{3+},zMn^{4+} and LZT$_{(1-y)}$:0.005Bi^{3+},yMn^{4+} all gradually enhance with increasing Mn^{4+} concentration (Fig. 11a and b). With regard to the LM$_{(1-w)}$Z$_w$T:0.005Bi^{3+},0.002Mn^{4+} (0 ≤ w ≤ 1) phosphors, the temperature-dependent PL intensity at 150 °C increases from 0.58 ($w = 1$) to 0.78 ($w = 0$) with the
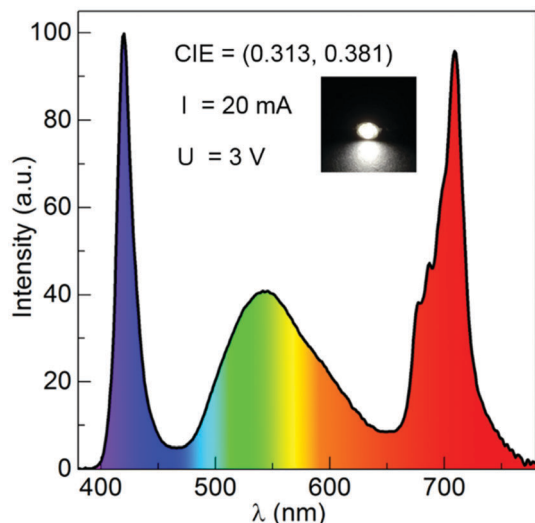
Fig. 12 Electroluminescence spectrum and luminescence photograph of a pc-WLEDs device fabricated using the commercially available green $Ba_3Si_6O_{12}N_2:Eu^{2+}$ phosphor and the representative red LZT:$0.005Bi^{3+}$,$0.002Mn^{4+}$ phosphor driven by an n-UV LED chip ($\lambda = 420$ nm).

increasing Mg^{2+} concentrations. Based on the previous discussion, decreasing the distortions of the [Zn/Mg/TiO$_6$] octahedra (Fig. S5, ESI†) will result in a greater local symmetry for Mn^{4+}-doping. Hence, the more Mg^{2+} ions are doped into the LM$_{(1-w)}$Z$_w$T:$0.005Bi^{3+}$,$0.002Mn^{4+}$ ($0 \leq w \leq 1$) phosphors, the more stable the structure is, which contributes to the enhancement of the thermal stability for the Mn^{4+} ion red emission (Fig. 11c). These results demonstrate that the non-radiative transition is weakened by an increase in the Mn^{4+} and Mg^{2+} concentration, which improves the thermal stability accordingly.

3.4 WLEDs application

To estimate the practical application of the as-prepared phosphors on pc-WLEDs devices, we fabricated a pc-WLEDs device by combining an n-UV LED chip ($\lambda = 420$ nm) and a mixture of the commercially available green $Ba_3Si_6O_{12}N_2:Eu^{2+}$ phosphor and the representative red LZT:$0.005Bi^{3+}$,$0.002Mn^{4+}$ phosphor. The performance of the fabricated pc-WLEDs and the luminescence photograph are show in Fig. 12. Under a voltage of 3.15 V and current of 20 mA, the obtained pc-WLEDs device exhibits a white emission with a low CCT (5825 K) and a high CIR ($R_a = 87.5$), of which the CIE coordinates are located at (0.3131, 0.3808). These results indicate that the as-prepared Bi^{3+}/Mn^{4+} co-doped LAT (A = Mg, Zn) double-perovskite phosphor could be an excellent red-emitting phosphor candidate for application in warm pc-WLEDs.

4. Conclusions

In this work, we have successfully synthesized a series of L$_{(1-u)}$MT:uBi^{3+}, LMT$_{(1-z)}$:zMn^{4+}, LMT$_{(1-z)}$:$0.005Bi^{3+}$,zMn^{4+}, L$_{(1-x)}$ZT:xBi^{3+},LZT$_{(1-y)}$:yMn^{4+}, LZT$_{(1-y)}$:$0.005Bi^{3+}$,yMn^{4+} and LM$_{(1-w)}$Z$_w$T:$0.005Bi^{3+}$,$0.002Mn^{4+}$ phosphors *via* a high-temperature

solid-state reaction in air. The Rietveld refinement clearly reveals that a phase transition from the orthorhombic cell (*Pbnm*) to the monoclinic cell ($P2_1/n$) exists in the La$_2$(Mg$_{1-w}$Zn$_w$)TiO$_6$:Bi^{3+},Mn^{4+} solid solution, resulting in a decreasing local structure symmetry of the [LaO$_{12}$] polyhedron from the '*m*' (C_s) symmetry to the lowest symmetry '1' (C_1) and an increasing crystal field distortion of the [Ti/Mg/ZnO$_6$] octahedra. Consequently, the PLE spectra of Mn^{4+} and the PL spectra of Bi^{3+} present a successive red shift. In addition, the energy transfers from Bi^{3+} to Mn^{4+} were successfully designed. The corresponding energy transfer efficiency can realize 93% for LMT$_{(1-z)}$:$0.005Bi^{3+}$,zMn^{4+} and 91% for LZT$_{(1-y)}$:$0.005Bi^{3+}$,yMn^{4+}. Moreover, this $Bi^{3+} \rightarrow Mn^{4+}$ energy transfer strategy could significantly improve the IQE values and the thermal stability. the IQE values increased from 31.5% (LMT:$0.002Mn^{4+}$) to 59.5% (LMT:$0.005Bi^{3+}$,$0.002Mn^{4+}$) and from 40.3% (LZT:$0.002Mn^{4+}$) to 70.8% (LZT:$0.005Bi^{3+}$,$0.002Mn^{4+}$), respectively. The performance of the fabricated pc-WLEDs devices indicates that LZT:$0.005Bi^{3+}$,$0.01Mn^{4+}$ could be a promising red phosphor for pc-WLEDs. This work offers an efficient strategy for designing $Bi^{3+} \rightarrow Mn^{4+}$ energy transfer in a double perovskite-type structure to improve the red emission of the Mn^{4+} ions and to achieve controllable color tuning for generating novel phosphors for application in pc-WLEDs.

Conflicts of interest

The authors declare no competing financial interest.

Acknowledgements

References

1 X. Qin, X. Liu, W. Huang, M. Bettinelli and X. Liu, *Chem. Rev.*, 2017, **117**, 4488–4527.
2 N. C. George, K. A. Denault and R. Seshadri, *Annu. Rev. Mater. Res.*, 2013, **43**, 481–501.
3 G. Li, Y. Tian, Y. Zhao and J. Lin, *Chem. Soc. Rev.*, 2015, **44**, 8688–8713.
4 L. Wang, R. J. Xie, T. Suehiro, T. Takeda and N. Hirosaki, *Chem. Rev.*, 2018, **118**, 1951–2009.
5 Z. Xia and Q. Liu, *Prog. Mater. Sci.*, 2016, **84**, 59–117.
6 C. C. Lin and R. S. Liu, *J. Phys. Chem. Lett.*, 2011, **2**, 1268–1277.

7 J. Ueda, P. Dorenbos, A. J. J. Bos, A. Meijerink and S. Tanabe, *J. Phys. Chem. C*, 2015, **119**, 25003–25008.

8 N. C. George, A. J. Pell, G. Dantelle, K. Page, A. Llobet, M. Balasubramanian, G. Pintacuda, B. F. Chmelka and R. Seshadri, *Chem. Mater.*, 2013, **25**, 3979–3995.

9 J. Zhong, W. Zhao, W. Zhuang, W. Xiao, Y. Zheng, F. Du and L. Wang, *ACS Omega*, 2017, **2**, 5935–5941.

10 J. Qiao, L. Ning, M. S. Molokeev, Y. C. Chuang, Q. Liu and Z. Xia, *J. Am. Chem. Soc.*, 2018, **140**, 9730–9736.

11 M. Zhao, H. Liao, L. Ning, Q. Zhang, Q. Liu and Z. Xia, *Adv. Mater.*, 2018, **30**, 1802489.

12 C. Y. Wang, T. Takeda, O. M. Ten Kate, M. Tansho, K. Deguchi, K. Takahashi, R. J. Xie, T. Shimizu and N. Hirosaki, *ACS Appl. Mater. Interfaces*, 2017, **9**, 22665–22675.

13 R. J. Xie, N. Hirosaki, T. Suehiro, F. F. Xu and M. Mitomo, *Chem. Mater.*, 2006, **18**, 5578–5583.

14 K. Sakuma, *IEICE Trans. Electron.*, 2005, **E88-C**, 2057–2064.

15 B. Deng, S. Liu, C. S. Zhou, H. Liu, J. Chen and R. Yu, *Chem. – Eur. J.*, 2018, **24**, 11627–11636.

16 P. Du, X. Huang and J. S. Yu, *Chem. Eng. J.*, 2018, **337**, 91–100.

17 H. Zhu, C. C. Lin, W. Luo, S. Shu, Z. Liu, Y. Liu, J. Kong, E. Ma, Y. Cao, R. S. Liu and X. Chen, *Nat. Commun.*, 2014, **5**, 4312.

18 M. H. Fang, W. L. Wu, Y. Jin, T. Lesniewski, S. Mahlik, M. Grinberg, M. G. Brik, A. M. Srivastava, C. Y. Chiang, W. Zhou, D. Jeong, S. H. Kim, G. Leniec, S. M. Kaczmarek, H. S. Sheu and R. S. Liu, *Angew. Chem., Int. Ed.*, 2018, **57**, 1797–1801.

19 K. Li, X. Liu, Y. Zhang, X. Li, H. Lian and J. Lin, *Inorg. Chem.*, 2015, **54**, 323–333.

20 H. Li, R. Pang, G. Liu, W. Sun, D. Li, L. Jiang, S. Zhang, C. Li, J. Feng and H. Zhang, *Inorg. Chem.*, 2018, **57**, 12303–12311.

21 G. Zhou, X. Jiang, J. Zhao, M. Molokeev, Z. Lin, Q. Liu and Z. Xia, *ACS Appl. Mater. Interfaces*, 2018, **10**, 24648–24655.

22 Z. Tan, J. Li, C. Zhang, Z. Li, Q. Hu, Z. Xiao, T. Kamiya, H. Hosono, G. Niu, E. Lifshitz, Y. Cheng and J. Tang, *Adv. Funct. Mater.*, 2018, **28**, 1801131.

23 F. Kang, H. Zhang, L. Wondraczek, X. Yang, Y. Zhang, D. Y. Lei and M. Peng, *Chem. Mater.*, 2016, **28**, 2692–2703.

24 F. Kang, M. Peng, D. Y. Lei and Q. Zhang, *Chem. Mater.*, 2016, **28**, 7807–7815.

25 F. Kang, M. Peng, X. Yang, G. Dong, G. Nie, W. Liang, S. Xu and J. Qiu, *J. Mater. Chem. C*, 2014, **2**, 6068–6076.

26 J. Han, L. Li, M. Peng, B. Huang, F. Pan, F. Kang, L. Li, J. Wang and B. Lei, *Chem. Mater.*, 2017, **29**, 8412–8424.

27 X. Li, P. Li, Z. Wang, S. Liu, Q. Bao, X. Meng, K. Qiu, Y. Li, Z. Li and Z. Yang, *Chem. Mater.*, 2017, **29**, 8792–8803.

28 J. Han, F. Pan, M. S. Molokeev, J. Dai, M. Peng, W. Zhou and J. Wang, *ACS Appl. Mater. Interfaces*, 2018, **10**, 13660–13668.

29 M. Sun, Q. He, X. Kuang, Q. Zhang, S. Ye and B. Huang, *Nano Energy*, 2018, **50**, 88–96.

30 Y. Zhu, Z. Qiu, B. Ai, Y. Lin, W. Zhou, J. Zhang, L. Yu, Q. Mi and S. Lian, *J. Lumin.*, 2018, **201**, 314–320.

31 Z. Zhou, Y. Zhong, M. Xia, N. Zhou, B. Lei, J. Wang and F. Wu, *J. Mater. Chem. C*, 2018, **6**, 8914–8922.

32 P. Dang, S. Liang, G. Li, Y. Wei, Z. Cheng, H. Lian, M. Shang, A. A. Al Kheraif and J. Lin, *Inorg. Chem.*, 2018, **57**, 9251–9259.

33 L. Li, Y. Pan, Z. Chen, S. Huang and M. Wu, *RSC Adv.*, 2017, **7**, 14868–14875.

34 H. R. Fuh, Y. P. Liu, Z. R. Xiao and Y. K. Wang, *J. Magn. Magn. Mater.*, 2014, **357**, 7–12.

35 J. Zhong, D. Chen, X. Chen, K. Wang, X. Li, Y. Zhu and Z. Ji, *Dalton Trans.*, 2018, **47**, 6528–6537.

36 J. Zhong, S. Zhou, D. Chen, J. Li, Y. Zhu, X. Li, L. Chen and Z. Ji, *Dalton Trans.*, 2018, **47**, 8248–8256.

37 K. Li, H. Lian and R. Van Deun, *Dalton Trans.*, 2018, **47**, 2501–2505.

38 Q. Sun, S. Wang, B. Devakumar, B. Li, L. Sun, J. Liang and X. Huang, *RSC Adv.*, 2018, **8**, 28538–28545.

39 J. Zhong, D. Chen, S. Yuan, M. Liu, Y. Yuan, Y. Zhu, X. Li and Z. Ji, *Inorg. Chem.*, 2018, **57**, 8978–8987.

40 Y. Takeda, H. Kato, M. Kobayashi, H. Kobayashi and M. Kakihana, *Chem. Lett.*, 2015, **44**, 1541–1543.

41 A. Meden and M. Čeh, *Mater. Sci. Forum*, 1998, **278–281**, 773–778.

42 C. K. Vigen, T. S. Bjørheim and R. Haugsrud, *Int. J. Hydrogen Energy*, 2012, **37**, 7983–7994.

43 A. Aguadero, J. A. Alonso, M. J. Martínez-Lope and M. T. Fernández-Díaz, *Solid State Sci.*, 2011, **13**, 13–18.

44 X. Wang, Z. Zhao, Q. Wu, Y. Li and Y. Wang, *Inorg. Chem.*, 2016, **55**, 11072–11077.

45 Y. Liu, J. Silver, R. J. Xie, J. Zhang, H. Xu, H. Shao, J. Jiang and H. Jiang, *J. Mater. Chem. C*, 2017, **5**, 12365–12377.

46 Y. Wei, L. Cao, L. Lv, G. Li, J. Hao, J. Gao, C. Su, C. C. Lin, H. S. Jang, P. Dang and J. Lin, *Chem. Mater.*, 2018, **30**, 2389–2399.

47 M. Zhao, Z. Xia, M. S. Molokeev, L. Ning and Q. Liu, *Chem. Mater.*, 2017, **29**, 6552–6559.

48 S. Liao, X. Ji, Y. Liu and J. Zhang, *ACS Appl. Mater. Interfaces*, 2018, **10**, 39064–39073.

49 W. L. Wu, M. H. Fang, W. Zhou, T. Lesniewski, S. Mahlik, M. Grinberg, M. G. Brik, H. S. Sheu, B. M. Cheng, J. Wang and R. S. Liu, *Chem. Mater.*, 2017, **29**, 935–939.

50 S. Adachi, *J. Lumin.*, 2018, **202**, 263–281.

51 Z. Zhang, C. Ma, R. Gautier, M. S. Molokeev, Q. Liu and Z. Xia, *Adv. Funct. Mater.*, 2018, 1804150, DOI: 10.1002/adfm.201804150.

52 Y. C. Fang, X. R. Huang, Y. D. Juang, S. Y. Chu and J. Ballato, *J. Am. Ceram. Soc.*, 2012, **95**, 1613–1618.

53 W. Xiao, X. Zhang, Z. Hao, G. H. Pan, Y. Luo, L. Zhang and J. Zhang, *Inorg. Chem.*, 2015, **54**, 3189–3195.

54 Z. Wang, W. Ye, I. H. Chu and S. P. Ong, *Chem. Mater.*, 2016, **28**, 8622–8630.

55 M. Zhang, Y. Liang, R. Tang, D. Yu, M. Tong, Q. Wang, Y. Zhu, X. Wu and G. Li, *RSC Adv.*, 2014, **4**, 40626–40637.

56 G. Li, Y. Wang, W. Zeng, W. Chen, S. Han, H. Guo and Y. Li, *J. Mater. Chem. C*, 2016, **4**, 3304–3312.

57 G. Li, Z. Hou, C. Peng, W. Wang, Z. Cheng, C. Li, H. Lian and J. Lin, *Adv. Funct. Mater.*, 2010, **20**, 3446–3456.

58 Y. H. Kim, P. Arunkumar, B. Y. Kim, S. Unithrattil, E. Kim, S. H. Moon, J. Y. Hyun, K. H. Kim, D. Lee, J. S. Lee and W. B. Im, *Nat. Mater.*, 2017, **16**, 543–550.

59 P. Strobel, C. Maak, V. Weiler, P. J. Schmidt and W. Schnick, *Angew. Chem., Int. Ed.*, 2018, **57**, 8739–8743.

60 S. K. Sharma, Y. C. Lin, I. Carrasco, T. Tingberg, M. Bettinelli and M. Karlsson, *J. Mater. Chem. C*, 2018, **6**, 8923–8933.